

A family of first-order accurate gradient schemes for finite volume methods

Oliver Oxtoby¹, Alexandros Syrakos^{*2}, Eugene de Villiers¹, Stylianos Varchanis², Yannis Dimakopoulos², and John Tsamopoulos²

¹*ENGYS, Studio 20, Royal Victoria Patriotic Building, John Archer Way, London, SW18 3SX, UK*

²*Laboratory of Fluid Mechanics and Rheology, Dept. of Chemical Engineering, University of Patras, 26500 Patras, Greece*

December 18, 2019

Abstract

A new discretisation scheme for the gradient operator, suitable for use in second-order accurate Finite Volume Methods (FVMs), is proposed. The derivation of this scheme, which we call the Taylor-Gauss (TG) gradient, is similar to that of the least-squares (LS) gradients, whereby the values of the differentiated variable at neighbouring cell centres are expanded in truncated Taylor series about the centre of the current cell, and the resulting equations are summed after being weighted by chosen vectors. Unlike in the LS gradients, the TG gradients use vectors aligned with the face normals, resembling the Green-Gauss (GG) gradients in this respect. Thus, the TG and LS gradients belong in a general unified framework, within which other gradients can also be derived. The similarity with the LS gradients allows us to try different weighting schemes (magnitudes of the weighting vectors) such as weighting by inverse distance or face area. The TG gradients are tested on a variety of grids such as structured, locally refined, randomly perturbed, and with high aspect ratio. They are shown to be at least first-order accurate in all cases, and are thus suitable for use in second-order accurate FVMs. In many cases they compare favourably over existing schemes.

1 Introduction

Gradient discretisation schemes are among the basic ingredients of Finite Volume Methods (FVMs) designed for grids of general geometry. They are used in the discretisation of diffusion [1, 2] and convection [3] terms, terms of turbulence closure equations [4], terms of non-Newtonian constitutive equations [3, 5–7] etc. Despite the level of maturity that FVMs have reached after decades of development, it has not yet been possible to devise a single general-purpose gradient discretisation scheme that performs well under all circumstances. The performance of each gradient scheme depends significantly on the geometrical characteristics of the grid in combination with the distribution of the differentiated variable. The main families of gradient schemes in use are the Green-Gauss (GG) gradients [4, 8–12], which are derived from the divergence (Gauss) theorem, and the least-squares (LS) gradients [11–16], which are derived from least-squares error minimisation.

*Corresponding author. E-mail address: alexandros.syrakos@gmail.com, syrakos@upatras.gr

In order for a FVM to be second-order accurate, it is necessary for the gradient schemes it employs to be at least first-order accurate. LS gradients share this property unconditionally on all types of grids [17], but GG gradients are, in general, zeroth-order accurate [17–19], unless special conditions hold. Such conditions, which grant first- or second-order accuracy, depend on the GG variant. They can be that the grid has no skewness [17] or lacks both skewness and unevenness (the face separating two cells not lying midway between the cell centres) [18] or is orthogonal [20]. Even if the grid does not possess these favourable geometrical properties, first- or second-order accuracy can be exhibited by GG gradients if it tends to acquire them through refinement [17]. Typically, GG gradients are first- or second-order accurate on smooth structured grids and zero-order accurate otherwise.

Despite this serious limitation of the GG gradients, they have remained very popular, partly because their inconsistency on general-geometry grids was not widely acknowledged until recently, but also partly because there is an important application where they are reputed to significantly outperform the LS gradients, namely in the simulation of high-speed boundary layer flows [21, 22]. In such flows, cells of very high aspect ratio are employed close to the solid boundary. If this boundary is curved, then the contours of the differentiated variable also curve along with the boundary and this nonlinear component of the variable’s variation can induce large errors in the LS gradient approximation [17]. GG gradients, on the other hand, not only become first-order accurate near the boundary due to the grid being structured there, but they additionally benefit from the alignment of the normal vectors of the long faces with the actual gradient of the differentiated variable to provide good accuracy.

So, each of these two gradient families has its own deficiencies. Efforts have been devoted to overcoming these deficiencies, including blending the two schemes [23]. For LS gradients, it has been observed that extending the computational molecule, i.e. also using information from neighbours that do not share a face with the cell where the gradient is sought, can bring good accuracy even on grids with high aspect ratio cells [19, 22]. The drawback is, of course, the additional computational cost and the increased coding complexity. Efforts have also been devoted to making the GG gradient consistent; these have mainly focused on using implicit formulae where the GG gradient at one cell also depends on the GG gradients at its neighbours. Then one either has to solve for all the gradients at all grid cells at once, solving a large linear system [24], or iterations have to be performed where the GG gradients at the neighbours are taken from the previous iteration (but these “gradient iterations” can be spread among the iterations of the PDE solver to drastically reduce the cost [17, 20]). In any case, overcoming the deficiencies of each of these gradient schemes comes at a cost.

In the present paper we propose a new gradient scheme that shares features with both the GG and LS gradients. In particular, like the LS gradients, it is at least first-order accurate on all grid geometries. It also shares with the GG gradients the feature that neighbour contributions are weighted by the corresponding face areas, which avoids excessive influence of small neighbours that can degrade the accuracy of LS gradients on locally refined meshes [17]. It is explicit, with no iterations or solutions of large linear systems being necessary. The scheme, which we call Taylor-Gauss (TG) gradient, is derived in a manner similar to the LS gradients, by expressing neighbour cell centre values as Taylor expansions with respect to the current cell centre, but then the resulting equations are weighted by the corresponding face normal vectors (similarly to the GG gradients) rather than by vectors pointing towards the neighbour cell centres (as in LS gradients). Thus, the new scheme and the LS schemes can be considered to be part of the same generalised framework.

The similarity between the TG and LS gradients naturally suggests that it may be beneficial to apply weights to the TG gradient equations, as in weighted LS schemes. Indeed, we show that there

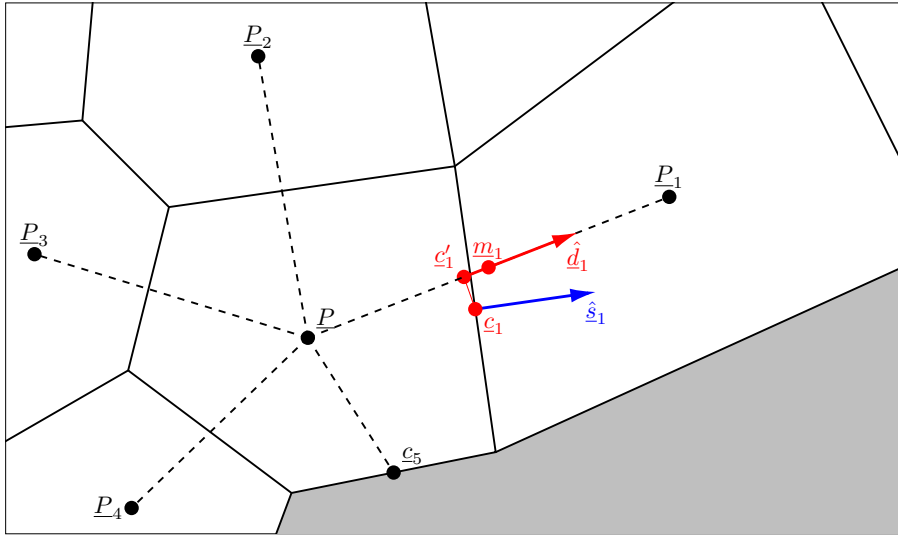


Figure 1: The notation adopted in the present paper.

exists a choice of weights that engenders second-order accuracy to the TG gradient on structured grids even at boundary cells, where most other schemes revert to first-order. This parallels a similar LS scheme that was studied in [17].

The general framework, within which both the LS and TG gradients can be derived, is presented in Sec. 2; all gradient schemes derived within this framework are shown to be at least first-order accurate. The derivation of the LS gradients within this framework is briefly presented in Sec. 3, and the Taylor-Gauss gradients are introduced in Sec. 4. In Sec. 4.4 it is shown that a particular TG variant becomes equivalent to the GG gradient when there is no grid skewness. The TG gradients are tested and compared against other schemes, such as the GG, skewness-corrected GG, LS, and variants of LS that incorporate area weighting, in Sec. 5. In Sec. 5.1 the gradient schemes are tested on grids that differ in terms of skewness and unevenness and whether these diminish with grid refinement (an analysis similar to that performed in [17]). In Sec. 5.2 the schemes are tested on grids of very high aspect ratio over curved boundaries. In each test case, the TG family includes members that are among the best-performing. Conclusions and ideas for further improvements are presented in Sec. 6.

2 General framework

In what follows, the notation illustrated in Fig. 1 will be used: we will try to calculate the gradient of a function ϕ at the centre \underline{P} of a cell under consideration. This cell has F faces, each of which separates it from a single neighbour cell, with the centroid of the neighbour across face f denoted as \underline{P}_f , or is a boundary face. Face f of this cell has centroid \underline{c}_f , whose projection on the line joining \underline{P} and \underline{P}_f is denoted as \underline{c}'_f . The point $\underline{m}_f = (\underline{P} + \underline{P}_f)/2$ lies midway between \underline{P} and \underline{P}_f . The distance vector from \underline{P} to \underline{P}_f is denoted as $\underline{D}_f = \underline{P}_f - \underline{P}$, and the unit vector in the same direction as $\hat{\underline{d}}_f = \underline{D}_f / \|\underline{D}_f\|$. The unit vector normal to face f is denoted by $\hat{\underline{s}}_f$, and if we multiply this by the face area S_f we get the face vector $\underline{S}_f = S_f \hat{\underline{s}}_f$.

We can define the following important grid quality metrics [17]: Skewness is the deviation of the centroid \underline{c}_f from the line joining \underline{P} and \underline{P}_f , and can be quantified as $\|\underline{c}_f - \underline{c}'_f\| / \|\underline{D}_f\|$; non-orthogonality is the angle between $\hat{\underline{d}}_f$ and $\hat{\underline{s}}_f$; and unevenness is the asymmetrical distancing of points \underline{P} and \underline{P}_f from face f , which can be quantified as $\|\underline{c}'_f - \underline{m}_f\| / \|\underline{D}_f\|$.

To begin, we choose a set of F points: $\underline{N}_1, \underline{N}_2, \dots, \underline{N}_F$; these are somehow related to the cell faces,

but the precise relationship does not matter at this point. We will calculate the value of $\nabla\phi$ at \underline{P} using the values of ϕ at \underline{P} itself and at the points \underline{N}_f . So, one possibility is to set $\underline{N}_f = \underline{P}_f$, since the values $\phi(\underline{N}_f)$ are considered known; points along the lines joining \underline{P} to \underline{P}_f , such as \underline{c}'_f and \underline{m}_f , are also attractive possibilities for \underline{N}_f as ϕ can be interpolated there to second-order accuracy. In the case of boundary faces, we can use the value of ϕ at the face centre, \underline{c}_f , assuming that the value of ϕ is known there. If it is not known there (e.g. ϕ is pressure, and we need to calculate $\nabla\phi$ to extrapolate pressure to the boundary) then we can actually exclude the boundary and use $F' < F$ points, as long as F' is large enough for the system that arises to have a unique solution (see below). In the following derivation it will be assumed that we use F points.

Next, we express $\phi(\underline{N}_f)$ in Taylor series about \underline{P} , to arrive at:

$$\Delta\phi_f = \underline{R}_f \cdot \nabla\phi(\underline{P}) + \frac{1}{2}\underline{R}_f\underline{R}_f : \nabla\nabla\phi(\underline{P}) + O(h^3) \quad (1)$$

where $\Delta\phi_f = \phi(\underline{N}_f) - \phi(\underline{P})$, $\underline{R}_f = \underline{N}_f - \underline{P}$, and h is a typical cell dimension. Throughout the paper, whenever vectors are written next to each other (e.g. $\underline{R}_f\underline{R}_f$ in the above equation), the tensor product between them is implied. If we drop the second- and higher-order terms of the above equations, then we are left with F equations with $D = 2$ or $D = 3$ unknowns (the components of $\nabla\phi(\underline{P})$), in two or three dimensional space, respectively.

For $F > D$ the system is over-determined. We can derive a full-rank $D \times D$ system from it by the following procedure. We first weigh (left-multiply) each equation (1) by a vector \underline{V}_f , to convert it into a vector equation:

$$\underline{V}_f\Delta\phi_f = \underline{V}_f\underline{R}_f \cdot \nabla\phi(\underline{P}) + \frac{1}{2}\underline{V}_f\underline{R}_f\underline{R}_f : \nabla\nabla\phi(\underline{P}) + O(\underline{V}_f) \cdot O(h^3) \quad (2)$$

Again, we have not particularised the choice of weighting vectors \underline{V}_f ; there is a plethora of legitimate choices, e.g. \underline{R}_f , $\hat{\underline{d}}_f$, $\underline{D}_f \hat{\underline{s}}_f$, \underline{S}_f , and many others.

We then sum all of the equations (2):

$$\sum_f \underline{V}_f\Delta\phi_f = \left[\sum_f \underline{V}_f\underline{R}_f \right] \cdot \nabla\phi(\underline{P}) + \frac{1}{2} \left[\sum_f \underline{V}_f\underline{R}_f\underline{R}_f \right] : \nabla\nabla\phi(\underline{P}) + O(\underline{V}_f) \cdot O(h^3) \quad (3)$$

Because $\underline{R}_f = O(h)$, we have $\underline{V}_f\underline{R}_f\underline{V}_f = O(\underline{V}_f) \cdot O(h^2)$. So, grouping together all terms of order 2 or higher and solving for $\nabla\phi(\underline{P})$ we obtain

$$\nabla\phi(\underline{P}) = \left[\sum_f \underline{V}_f\underline{R}_f \right]^{-1} \cdot \left[\sum_f \underline{V}_f\Delta\phi_f \right] + \underbrace{\left[\sum_f \underline{V}_f\underline{R}_f \right]^{-1} \cdot O(\underline{V}_f) \cdot O(h^2)}_{= [O(\underline{V}_f)O(h)]^{-1} \cdot O(\underline{V}_f)O(h^2) = O(h)} \quad (4)$$

So, the first term on the right-hand side gives us an (at least) first-order accurate gradient. It is also exact for linear functions, as can be seen from Eq. (3), where in the case of a linear function $\nabla\nabla\phi$ and all the higher derivatives are zero.

Necessary conditions on \underline{R}_f and \underline{V}_f

The gradient calculation (4) requires that the matrix $\sum_f \underline{V}_f \underline{R}_f$ be invertible. In order for that to hold, the $D \times D$ matrix must be of full rank, i.e. it must have linearly independent columns and linearly independent rows. Obviously each of the component matrices $\underline{V}_f \underline{R}_f$ has rank 1 and is singular, but their sum may be of full rank. The columns of $\sum_f \underline{V}_f \underline{R}_f$ are linear combinations of the vectors \underline{V}_f , and therefore in order to have D linearly independent columns we need at least D linearly independent vectors \underline{V}_f (in fact we can't have more than D in D -dimensional space). Similarly, for $\sum_f \underline{V}_f \underline{R}_f$ to have D linearly independent rows we need D linearly independent vectors \underline{R}_f . To summarise: in D -dimensional space we need at least D neighbouring points \underline{N}_f , such that there is at least one subset of them with D points whose \underline{R}_f vectors are linearly independent (span \mathbb{R}^D), with the corresponding \underline{V}_f vectors also being linearly independent.

What if the values at \underline{N}_f are interpolated?

In the above analysis we have assumed that $\Delta\phi$ are exact, i.e. that $\phi(\underline{N}_f)$ is the exact value of ϕ at point \underline{N}_f . But what if we only have approximate values of ϕ at the points \underline{N}_f ? In particular, suppose that we have obtained by some interpolation scheme approximate values $\phi^*(\underline{N}_f) = \phi(\underline{N}_f) + O(h^p) \Rightarrow \Delta\phi_f^* = \Delta\phi_f + O(h^p)$. Substituting this into Eq. (4) we get:

$$\begin{aligned} \nabla\phi(\underline{P}) &= \left[\sum_f \underline{V}_f \underline{R}_f \right]^{-1} \cdot \left[\sum_f \underline{V}_f (\Delta\phi_f^* + O(h^p)) \right] + O(h) \\ &= \left[\sum_f \underline{V}_f \underline{R}_f \right]^{-1} \cdot \left[\sum_f \underline{V}_f \Delta\phi_f^* \right] + \underbrace{\left[\sum_f \underline{V}_f \underline{R}_f \right]^{-1} \cdot \left[\sum_f \underline{V}_f O(h^p) \right]}_{= [O(\underline{V}_f)O(h)]^{-1} \cdot O(\underline{V}_f)O(h^p) = O(h^{p-1})} + O(h) \end{aligned} \quad (5)$$

Therefore, in order to have a first-order accurate gradient we need to have $p \geq 2$, i.e. at least second-order accurate interpolations at the points \underline{N}_f . This excludes the possibility of using first-order upwinding (UDS) at $\underline{N}_f = \underline{c}'_f$.

Next, we turn to some particular choices for \underline{N}_f and \underline{V}_f .

3 The least-squares sub-family of gradients

Let us choose $\underline{N}_f = \underline{P}_f$. In this case, $\underline{R}_f = \underline{D}_f = [R_{f,x}, R_{f,y}, R_{f,z}]^T$, say, in component form. The least squares gradients come from solving the following system in the least squares sense [17]:

$$\underbrace{\begin{bmatrix} w_1 & & & \\ & w_2 & & \\ & & \ddots & \\ & & & w_F \end{bmatrix}}_W \cdot \underbrace{\begin{bmatrix} R_{1,x} & R_{1,y} & R_{1,z} \\ R_{2,x} & R_{2,y} & R_{2,z} \\ \vdots & \vdots & \vdots \\ R_{F,x} & R_{F,y} & R_{F,z} \end{bmatrix}}_A \cdot \underbrace{\begin{bmatrix} \phi_x(\underline{P}) \\ \phi_y(\underline{P}) \\ \phi_z(\underline{P}) \end{bmatrix}}_x = \underbrace{\begin{bmatrix} w_1 & & & \\ & w_2 & & \\ & & \ddots & \\ & & & w_F \end{bmatrix}}_W \cdot \underbrace{\begin{bmatrix} \Delta\phi_1 \\ \Delta\phi_2 \\ \vdots \\ \Delta\phi_F \end{bmatrix}}_b \quad (6)$$

where $\nabla\phi(\underline{P}) = [\phi_x(\underline{P}), \phi_y(\underline{P}), \phi_z(\underline{P})]^T$ and w_f is the weight applied to equation f of the system. In order to solve the over-determined system $WAx = Wb$ in the least squares sense, we solve the normal

equations $(WA)^T(WA)x = (WA)^TWb \Rightarrow A^TW^2Ax = A^TW^2b$. This can be expanded as

$$\underbrace{\begin{bmatrix} | & | & & | \\ w_1^2 \underline{R}_1 & w_2^2 \underline{R}_2 & \cdots & w_F^2 \underline{R}_F \\ | & | & & | \end{bmatrix}}_{\underline{V}_f = w_f^2 \underline{R}_f} \begin{bmatrix} -\underline{R}_1 \\ -\underline{R}_2 \\ \vdots \\ -\underline{R}_F \end{bmatrix} \begin{bmatrix} \phi_x(\underline{P}) \\ \phi_y(\underline{P}) \\ \phi_z(\underline{P}) \end{bmatrix} = \underbrace{\begin{bmatrix} | & | & & | \\ w_1^2 \underline{R}_1 & w_2^2 \underline{R}_2 & \cdots & w_F^2 \underline{R}_F \\ | & | & & | \end{bmatrix}}_{\underline{V}_f = w_f^2 \underline{R}_f} \begin{bmatrix} \Delta\phi_1 \\ \Delta\phi_2 \\ \vdots \\ \Delta\phi_F \end{bmatrix}$$

The above is equivalent to

$$\left[\sum_f w_f^2 \underline{R}_f \underline{R}_f^T \right] \cdot \nabla\phi(\underline{P}) = \sum_f w_f^2 \underline{R}_f \Delta\phi_f$$

which gives, using tensor notation to drop the transpose symbol,

$$\nabla\phi(\underline{P}) = \left[\sum_f w_f^2 \underline{R}_f \underline{R}_f \right]^{-1} \left[\sum_f w_f^2 \underline{R}_f \Delta\phi_f \right] \quad (7)$$

Comparing Eqs. (7) and (4) we see that the least squares methods are a special case of the framework presented here, with $\underline{N}_f = \underline{P}_f$ and $\underline{V}_f = w_f^2 \underline{R}_f$. For example:

- $w_f = 1$ (unweighted method): $\underline{V}_f = \underline{R}_f = \|\underline{R}_f\| \hat{\underline{d}}_f$
- $w_f = \|\underline{R}_f\|^{-1}$ (“ $q = 1$ ” weighted method in [17]): $\underline{V}_f = \|\underline{R}_f\|^{-2} \underline{R}_f = \|\underline{R}_f\|^{-1} \hat{\underline{d}}_f$
- $w_f = \|\underline{R}_f\|^{-3/2}$ (“ $q = 3/2$ ” weighted method in [17]): $\underline{V}_f = \|\underline{R}_f\|^{-3} \underline{R}_f = \|\underline{R}_f\|^{-2} \hat{\underline{d}}_f$

In what follows, we will denote as LS(q) the gradient with $\underline{V}_f = \|\underline{R}_f\|^{-q} \hat{\underline{d}}_f$. Note that the use of q is different here than in [17]; for example, the LS(-1), LS(1) and LS(2) are the “ $q = 0$ ” (unweighted), “ $q = 1$ ” and “ $q = 3/2$ ” methods of [17], respectively. We will also test some face area-weighted least squares variants in some of the tests of Sec. 5; in particular, we will denote as LSA(q) the gradient with $\underline{V}_f = S_f \|\underline{R}_f\|^{-q} \hat{\underline{d}}_f$.

4 Taylor-Gauss gradients

Suppose now that we pick our points \underline{N}_f somewhere along the lines joining \underline{P} to \underline{P}_f , so that we can calculate ϕ there with at least second-order accuracy (linear interpolation). Possible choices include \underline{P}_f , \underline{c}'_f and \underline{m}_f ; the particular choice is not important at this stage, and will be investigated later.

The important choice here is the vectors \underline{V}_f , which we choose to be in the directions of the face normals. So, let us choose as a first option $\underline{V}_f = \underline{S}_f$. According to Eq. (4), the scheme, which we call “Taylor-Gauss” gradient, becomes:

$$\nabla\phi(\underline{P}) = \left[\sum_f \underline{S}_f \underline{R}_f \right]^{-1} \left[\sum_f \underline{S}_f \Delta\phi_f \right] \quad (8)$$

4.1 Magnitudes of the weight vectors \underline{V}_f

The foundation of the Taylor-Gauss family is the alignment of the weight vectors \underline{V}_f with the face normals \hat{s}_f . This leaves flexibility in the choice of the magnitudes of \underline{V}_f . In the formulation (8), the weight vectors $\underline{V}_f = \underline{S}_f = S_f \hat{s}_f$ are weighted by the face areas S_f . This was shown in [17] to be a positive feature, as it avoids excessive weighting on sides of a cell where there are many small neighbour cells (e.g. in locally refined grids). On high aspect ratio cells, S_f is large on the long faces and small on the short faces; it also happens that neighbours across the long faces are closer to \underline{P} than neighbours across the short faces. Therefore, weighing by S_f has a similar effect as weighing with $\|\underline{R}_f\|^{-1}$. We will consider a more general weighing scheme (similar to the LSA gradients):

$$\underline{V}_f = \frac{S_f}{\|\underline{R}_f\|^q} \hat{s}_f \quad (9)$$

4.2 Choice of points \underline{N}_f

In Eq. (8) we have not yet specified the choice of \underline{N}_f (and hence of \underline{R}_f). A straightforward choice would be $\underline{N}_f = \underline{P}_f$, the neighbour cell centroids, just like in the least squares gradients. In the traditional GG gradients, sometimes the points $\underline{m}_f = (1/2)(\underline{P} + \underline{P}_f)$ are used; this results in $\underline{R}_f|_{\underline{N}_f=\underline{m}_f} = (1/2)\underline{R}_f|_{\underline{N}_f=\underline{P}_f}$ where the subscript after the “|” denotes the conditions under which \underline{R}_f is defined. If the values of ϕ at points \underline{m}_f are calculated using linear interpolation, then we similarly have $\Delta\phi_f|_{\underline{N}_f=\underline{m}_f} = (1/2)\Delta\phi_f|_{\underline{N}_f=\underline{P}_f}$. Because the (1/2) factors of these two relations cancel out, it turns out that it doesn’t matter at all whether we use \underline{P}_f or \underline{m}_f as the \underline{N}_f points; the result is exactly the same:

$$\begin{aligned} \nabla\phi(\underline{P}) &= \left[\sum_f \underline{S}_f \underline{R}_f|_{\underline{N}_f=\underline{m}_f} \right]^{-1} \left[\sum_f \underline{S}_f \Delta\phi_f|_{\underline{N}_f=\underline{m}_f} \right] \\ &= \left[\sum_f \underline{S}_f \underline{R}_f|_{\underline{N}_f=\underline{P}_f} \right]^{-1} \left[\sum_f \underline{S}_f \Delta\phi_f|_{\underline{N}_f=\underline{P}_f} \right] \end{aligned}$$

This occurs because the factor (1/2) is common between all faces; similarly, any other such fixed factor (e.g. (1/3) etc.) would make no difference; the increased accuracy of using closer points \underline{m}_f instead of \underline{P}_f is exactly offset by the added linear interpolation error.

On the other hand, if $\underline{N}_f = \underline{c}'_f$ are used instead, then the interpolation factors are different for each face and such cancellation does not occur, giving a slightly different result than using $\underline{N}_f = \underline{P}_f$. In the following, we will denote as TG(q) the scheme with $\underline{N}_f = \underline{P}_f$ and \underline{V}_f given by Eq. (9), and as iTG(q) the scheme with $\underline{N}_f = \underline{c}'_f$ and linear interpolation to obtain $\phi(\underline{c}'_f)$ (an “interpolated” version of TG), the weighting vectors again given by Eq. (9).

We can also note that iTG(1) is completely equivalent to TG(1). Indeed, if we denote $\alpha_f = \|\underline{c}'_f - \underline{P}\|/\|\underline{P}_f - \underline{P}\|$ then

$$\begin{aligned} \underline{c}'_f &= (1 - \alpha_f)\underline{P} + \alpha_f\underline{P}_f & \Rightarrow \underline{R}_f|_{\underline{N}_f=\underline{c}'_f} &= \alpha_f \underline{R}_f|_{\underline{N}_f=\underline{P}_f} \\ \phi(\underline{c}'_f) &\approx (1 - \alpha_f)\phi(\underline{P}) + \alpha_f\phi(\underline{P}_f) & \Rightarrow \Delta\phi_f|_{\underline{N}_f=\underline{c}'_f} &= \alpha_f \Delta\phi_f|_{\underline{N}_f=\underline{P}_f} \end{aligned}$$

Substituting the above relations into the expression (4) for the iTG(1) gradient, the α_f factors cancel out and we are left with the expression for the TG(1) gradient.

4.3 Increasing the order near boundaries

It would be nice if we had a method analogous to the “ $q = 3/2$ ” least-squares method of [17], which retains second-order accuracy at boundary cells of structured grids. In fact this is possible. Let us set $\underline{N}_f = \underline{P}_f$ so we don’t have to worry about interpolation error. From Eq. (3) we see that in order to get a 2nd-order accurate gradient we need that $\sum_f \underline{V}_f \underline{R}_f \underline{R}_f = 0$. This can be achieved under special circumstances with an appropriate choice of \underline{V}_f .

The (i, j, k) component of the third order tensor $\sum_f \underline{V}_f \underline{R}_f \underline{R}_f$ is $\sum_f \underline{V}_{f,i} \underline{R}_{f,j} \underline{R}_{f,k}$. With \underline{V}_f given by Eq. (9), these components become

$$\sum_f \underline{V}_{f,i} \underline{R}_{f,j} \underline{R}_{f,k} = \sum_f \frac{S_f}{\|\underline{R}_f\|^q} (\hat{s}_f \cdot \hat{e}_i) R_{f,j} R_{f,k} \quad (10)$$

where \hat{e}_i is the unit vector in the i -th coordinate direction, and the components of \underline{R}_f are denoted as $[R_{f,1}, R_{f,2}, R_{f,3}]$.

Now consider a structured grid, generated by solving a set of PDEs, so that grid refinement causes skewness to diminish and cells to tend to become parallelograms / parallelepipeds [17]. The “ $q = 3/2$ ” least squares gradient of [17] (LS(2) in the present notation) is second order accurate even at boundary cells of such grids, despite the distance between \underline{P} and the boundary face centroid being about half that between \underline{P} and the neighbour cell centroid across the opposite face. The same is achieved by the Taylor-Gauss scheme if we choose $q = 2$ in (9). Indeed, for two opposite faces on such a grid, say $f = 1$ and $f = 2$, we have $S_1 = S_2$, $\hat{s}_1 = -\hat{s}_2$, and $R_{1,j}/\|\underline{R}_1\| = -R_{2,j}/\|\underline{R}_2\|$ because the vectors \underline{R}_1 and \underline{R}_2 are parallel but point in opposite directions, and these ratios are the cosine of an angle related to this common direction. Therefore, the contributions of these two faces in the sum (10) cancel out:

$$S_1 (\hat{s}_1 \cdot \hat{e}_i) \frac{R_{1,j}}{\|\underline{R}_1\|} \frac{R_{1,k}}{\|\underline{R}_1\|} + S_2 (\hat{s}_2 \cdot \hat{e}_i) \frac{R_{2,j}}{\|\underline{R}_2\|} \frac{R_{2,k}}{\|\underline{R}_2\|} = 0 \quad (11)$$

Thus, on such a grid with $q = 2$ the leading error components in each pair of opposite faces cancel out, and we are left with a second-order accurate Taylor Gauss gradient, TG(2), even at the boundary cells. In exactly the same way it can be shown that LSA(2) is second-order accurate under these circumstances (the only difference is that \hat{d}_f instead of \hat{s}_f appear in Eq. (11)). Thus, this property is shared by all three schemes LS(2), LSA(2) and TG(2).

4.4 Relationship between the Taylor-Gauss and Green-Gauss gradients

As mentioned in Sec. 1, the new family of gradients was named “Taylor-Gauss” because they are based on Taylor expansions of the neighbouring values, but the equations are weighted by vectors that are perpendicular to the cell faces, so that the scheme bears some resemblance to the Green-Gauss gradients, a popular variant of which is

$$\nabla \phi(\underline{P}) = \frac{1}{\Omega_P} \sum_f \underline{S}_f \phi(\underline{c}'_f) \quad (12)$$

where Ω_P is the cell volume. The resemblance to iTG(0) can be made more apparent by noticing that the the right-hand side vector in (8) can be written as

$$\sum_f \underline{S}_f \Delta \phi_f = \sum_f \underline{S}_f (\phi(\underline{c}'_f) - \phi(\underline{P})) = \sum_f \underline{S}_f \phi(\underline{c}'_f) - \phi(\underline{P}) \sum_f \underline{S}_f = \sum_f \underline{S}_f \phi(\underline{c}'_f)$$

because $\sum_f \underline{S}_f = 0$. Thus the iTG(0) (8) and GG (12) gradients differ only in that this vector is left-multiplied by $[\sum_f \underline{S}_f \underline{R}_f]^{-1}$ in the former and by $\Omega_P^{-1} \underline{I}$ in the latter, where \underline{I} is the identity tensor.

In the absence of skewness, $\underline{c}'_f = \underline{c}_f$, and it turns out that the iTG(0) and GG gradients become equivalent because $\sum_f \underline{S}_f \underline{R}_f = \Omega_P \underline{I}$. This can be shown as follows: consider a coordinate system with origin at \underline{P} , with x_i being the i -th coordinate direction and \hat{e}_i the corresponding unit vector. Then

$$\nabla \cdot (x_i \hat{e}_j) = \delta_{ij} \Rightarrow \int_{\Omega_P} \nabla \cdot (x_i \hat{e}_j) d\Omega = \int_{\Omega_P} \delta_{ij} d\Omega = \delta_{ij} \Omega_P \quad (13)$$

The integral of Eq. (13) can also be evaluated using the divergence (Gauss) theorem:

$$\int_{\Omega_P} \nabla \cdot (x_i \hat{e}_j) d\Omega = \int_{S_P} x_i \hat{e}_j \cdot \hat{n} ds = \sum_f \hat{e}_j \cdot \hat{n}_f \int_{S_f} x_i ds = \sum_f \hat{e}_j \cdot \underline{S}_f R_{f,i} \quad (14)$$

where S_P is the surface of cell Ω_P , ds is an infinitesimal element of that surface, and \hat{n} is the outward normal unit vector, which is constant and equal to \hat{n}_f over each face f . In the last equality of Eq. (14) we have used that $\int_{S_f} x_i ds = S_f c_{f,i}$, with $c_{f,i}$ being the i -th coordinate of the centroid \underline{c}_f , by definition of the centroid. The latter also equals $R_{f,i}$, the i -th coordinate of $\underline{R}_f = \underline{c}_f - \underline{P}$, because $\underline{P} = 0$ is the coordinates' origin. Thus Eq. (14) becomes $\sum_f S_{f,j} R_{f,i}$, i.e. the (j, i) of the matrix $\sum_f \underline{S}_f \underline{R}_f$. This is equal to $\delta_{ji} \Omega_P$, the (j, i) component of the matrix $\Omega_P \underline{I}$, by Eq. (13). Therefore the two matrices are equal and the iTG(0) gradient is equivalent to the GG gradient.

In the presence of skewness ($\underline{c}'_f \neq \underline{c}_f$) the two methods are not equivalent, with the GG gradient becoming inconsistent (unless skewness diminishes with grid refinement [17]) whereas the iTG(0) retains its first-order accuracy. Note that even if $\underline{c}'_f = \underline{c}_f$ the TG gradients, unlike the GG gradients, have the freedom of not using all F faces of the cell, because their derivation is not founded on the divergence theorem. For example, if the gradient is used for extrapolating a variable (e.g. pressure or stress) to a boundary, then the boundary face itself may be omitted from the gradient calculation. In this case the matrix $\sum_f \underline{S}_f \underline{R}_f$ of iTG(0) is not equal to the matrix $\Omega_P \underline{I}$ of GG.

5 Results

5.1 Order of accuracy

In this section we apply some of the new gradient schemes to calculate the gradient of the function $\phi(x, y) = \tanh(x) \cdot \tanh(y)$, on the domains and grids shown in Fig. 2. The same tests were conducted in [17] to test the GG and LS schemes, and therefore the setup of the tests will be briefly summarised here, while more details can be found in [17]. The selected grids exhibit different qualities in terms of skewness and unevenness and the way these change with grid refinement. The analysis of [17] showed that these qualities can affect the observed order of accuracy of a gradient scheme (non-orthogonality can also affect the observed order of accuracy of some gradient schemes [20], but not of the ones examined here). For each kind of grid, we use 8 different levels of refinement ($l = 0, 1, \dots, 7$), with each successive grid having four times as many cells as the previous one. The grids of Fig. 2 correspond to the second level of refinement. The distinguishing features of these grids are:

- The grid of Fig. 2a is a structured grid that was generated by solving a set of elliptic partial differential equations (see [17] for details). Such grids are characterised by skewness and unevenness that diminish towards zero through grid refinement. All gradient schemes, including the

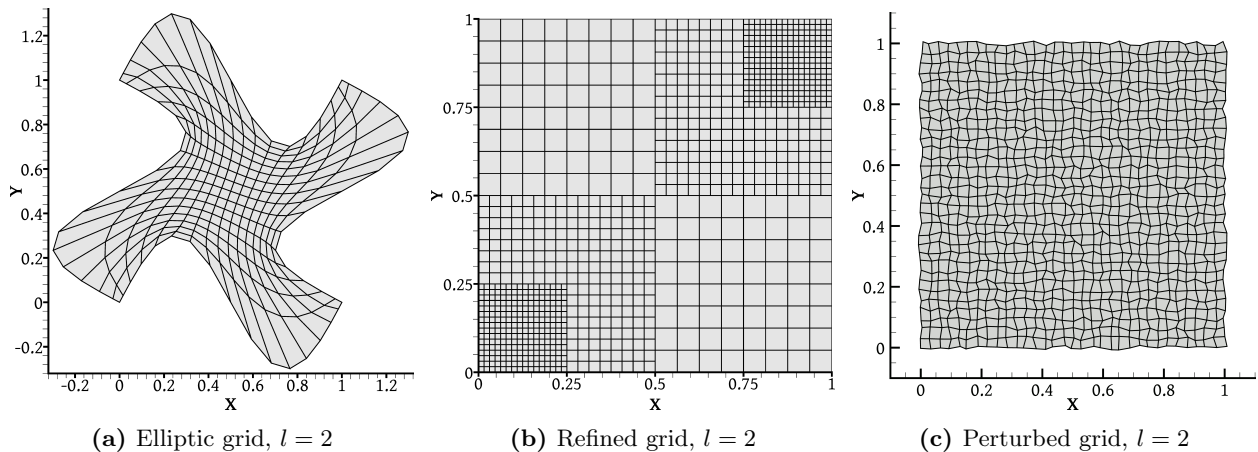


Figure 2: Grids of different kinds, at the $l = 2$ level of refinement.

GG gradient, are expected to exhibit second-order accuracy at all interior cells, and first-order accuracy at boundary cells except for the LS(2), LSA(2) and TG(2) gradients which should remain second-order accurate there.

- The grid of Fig. 2b is a Cartesian grid with local refinement patches. Skewness is everywhere zero except at the patch interfaces where it has large values. Finer grids are obtained by splitting each cell, including those of the patches, into four smaller cells. Therefore, all finer grids are similarly patched, and the skewness at the patch interfaces remains the same on all grids. Unevenness is non-zero and non-diminishing at patch interfaces and boundary cells. All gradients are expected to be second-order accurate in uniform parts of the grid and first-order accurate (the GG gradients are zeroth-order accurate) in cells adjacent to the patch interfaces. In boundary cells, the LS(2), LSA(2) and TG(2) gradients are expected to be second-order accurate and all other gradients first-order accurate.
- The grid of Fig. 2c is a Cartesian grid whose nodes have been perturbed by a random displacement – see [17] for details. Skewness and unevenness are large and, on average, non-diminishing with refinement. All gradient schemes are expected to be first-order accurate, except the GG gradients which are zeroth-order accurate.

The mean and maximum of the errors $\|\nabla^a\phi(\underline{P}) - \nabla\phi(\underline{P})\|$ across all grid cells, where ∇^a is the approximate gradient and $\nabla\phi$ is the exact gradient, are plotted in Figs. 3–5. In order not to clutter the diagrams, we plot the errors of only a subset of the schemes we tested. The tested gradients include iTG(q), TG(q), and LSA(q) for $q = 0, 1$ and 2. For comparison, we include the results for the LS(-1), LS(1), LS(2) and uncorrected GG gradients from [17]. We also tested two corrected versions of the GG gradient; skewness correction can make the GG gradient consistent, but even on structured grids, where the GG gradient is already second-order accurate (except at the boundary), it was shown in [17] that such correction can improve the accuracy significantly. In the present work, we chose to test skewness-corrected GG gradients, denoted as GG+iTG(0) and GG+LS(1), where the skewness correction is calculated using either the iTG(0) or LS(1) gradients, respectively. This avoids the need for iterations, which are necessary if GG itself is used for the correction [17]. In particular, the corrected GG gradient is computed as

$$\nabla\phi(\underline{P}) = \frac{1}{\Omega_P} \sum_f \underline{S}_f\phi(\underline{c}_f) \quad (15)$$

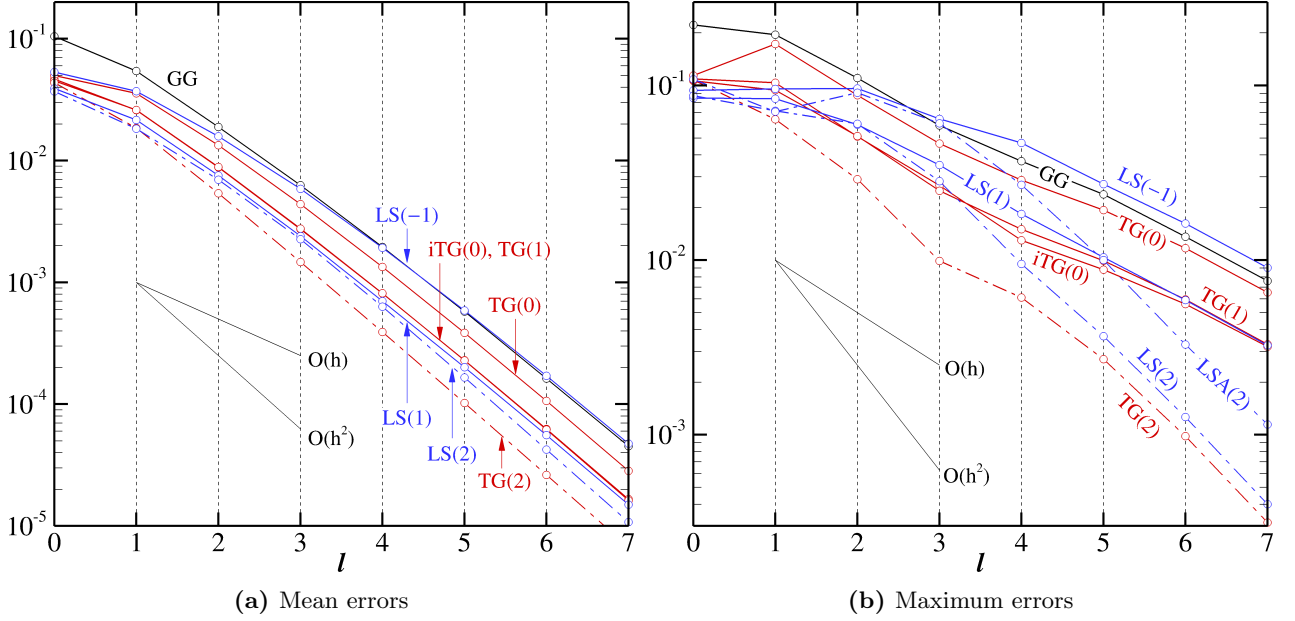


Figure 3: Minimum and maximum errors of gradient schemes versus refinement level l , for the elliptic grids (Fig. 2a).

where $\phi(\underline{c}_f)$ is approximated as

$$\phi(\underline{c}_f) = \phi(\underline{c}'_f) + \nabla\phi(\underline{c}'_f) \cdot (\underline{c}_f - \underline{c}'_f) \quad (16)$$

In Eq. (16), both $\phi(\underline{c}'_f)$ and $\nabla\phi(\underline{c}'_f)$ are calculated using linear interpolation between points \underline{P} and \underline{P}_f . If the gradient in (16) is at least first-order accurate, such as the chosen iTG(0) and LS(1), then the interpolation (16) is second-order accurate, and the resulting GG+iTG(0) and GG+LS(1) gradients (15) are also at least first-order accurate. Skewness-corrected GG gradients, deriving from the divergence theorem, have the property of being “conservative”, in the sense that e.g. if the pressure force on a cell is discretised as $\nabla p(\underline{P}) \Omega_P$, then such gradients result in each face contributing by equal and opposite amounts to the pressure forces on the cells that share it (face f contributes equally, but in the opposite direction, to $\nabla p(\underline{P}) \Omega_P$ and $\nabla p(\underline{P}_f) \Omega_{P_f}$). LS and TG gradients do not have this property.

On the smooth structured grids (Fig. 3), as expected, the mean errors of all schemes decrease at a second-order rate (Fig. 3a), because skewness diminishes with refinement [17]. The maximum errors (Fig. 3b), which occur at boundary cells, reduce at a first-order rate, except for the LS(2), LSA(2) and TG(2) gradients which are second-order accurate even there. The most accurate gradient overall is the TG(2) followed by LS(2); the least accurate are the LS(-1) (unweighted least squares) and GG, followed by the TG(0) and LSA(0) (not shown). The performances of the rest of the gradient schemes are very similar and lie in between. GG+iTG(0) and GG+LS(1) have similar performance to LS(1), which confirms the accuracy boost that GG receives through skewness correction. Among the $q = 2$ schemes, the LSA(2) is the worst performer with an mean accuracy (not shown) that is comparable to that of TG(1) down to level $l = 7$.

On the locally refined grids (Fig. 4), the mean errors of all methods (except the GG, whose errors are not shown because they do not decrease with refinement – the results can be found in [17]) decrease at a second-order rate (Fig. 4a). Of course, the errors at cells touching patch interfaces, and for most methods also at boundary cells, decrease only at a first-order rate (Fig. 4b), but because the number of

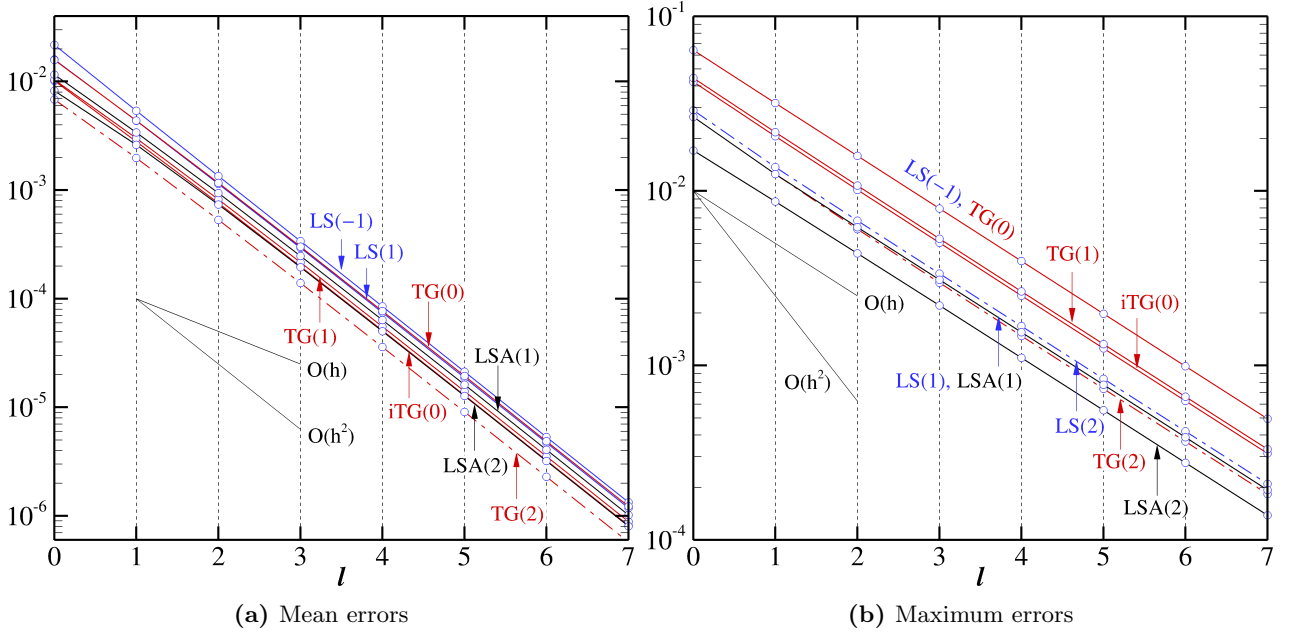


Figure 4: Minimum and maximum errors of various gradients versus refinement level l , for the locally refined grids (Fig. 2b).

such cells as a proportion of the total number of cells diminishes with refinement, the mean errors still decrease at a second-order rate [17]. Figure 4a shows that there are no large differences in performance between the methods; nevertheless, one may notice that the group of worst-performance methods now includes LS(1) in addition to LS(-1) and TG(0). In [17] it was shown that on locally refined grids, at cells which touch a finer patch, the least-squares methods suffer a modest accuracy decline because they overvalue information on the fine patch, where there are more than one neighbour cells, compared to information on the other side where there is only one coarse-patch cell. Face area weighting should mitigate this problem, as the increased number of neighbours on the fine patch will be counterbalanced by the smaller area of the corresponding faces. Indeed, Fig. 4a shows that the LSA(1) and LSA(2) gradients perform better than LS(1). Even so, the LSA methods still slightly underperform compared to the TG methods on average. On the other hand, LSA methods perform very good with respect to the maximum error (Fig. 4b).

Finally, on the randomly perturbed grids (Fig. 5), all methods (excluding the zeroth-order accurate GG methods, which are not plotted) are first-order accurate. Neither the mean nor the maximum errors differ greatly among the various schemes. The LS(-1) and TG(0) methods are again the worst performers among those tested, while the TG(2) gradient performs best.

So, overall, most of the gradient schemes tested have similar performance. The ones that stand out for their bad performance are the uncorrected GG and the LS(-1). The TG(0), although markedly better than these two, clearly lags behind the other gradients in terms of accuracy. The $q = 2$ gradients benefit from increased accuracy at boundaries when the circumstances are favourable, but the LSA(2) in general performs worse compared to LS(2) and TG(2). TG(2) is the best overall performer in the present tests.

5.2 Performance on curved high-aspect ratio grids

The results of Sec. 5.1 showed that most of the TG and LS variants, except the unweighted LS(-1) and, to some degree, TG(0), have similar performance and would be satisfactory for use in second-

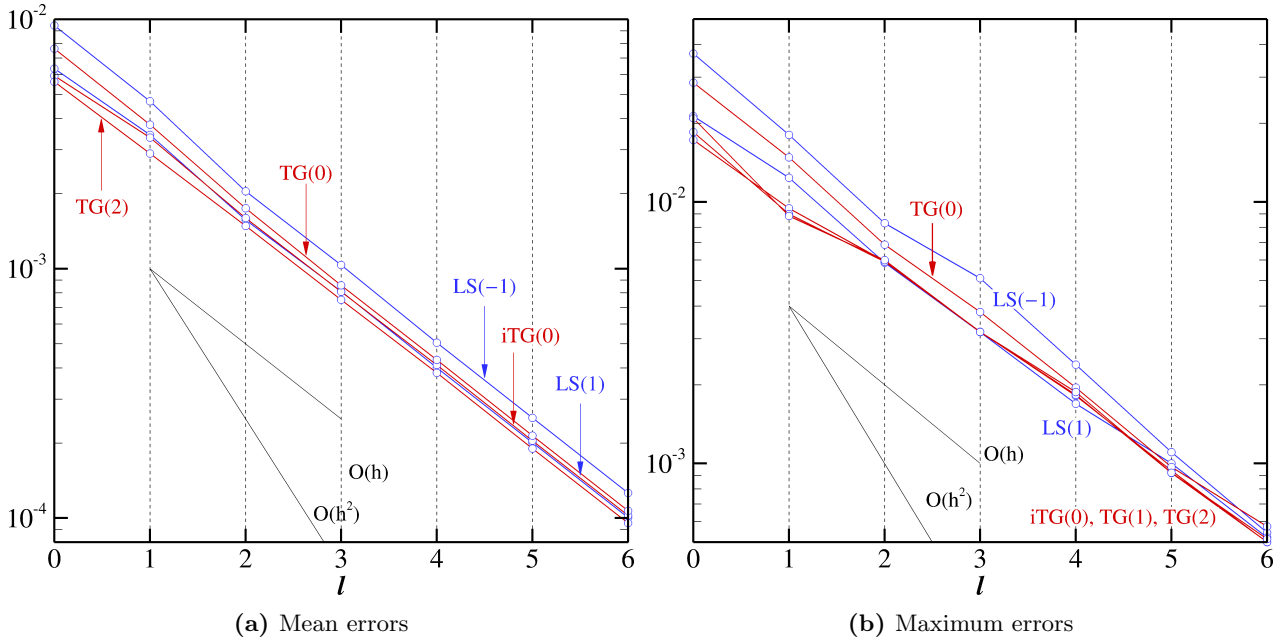


Figure 5: Minimum and maximum errors of various gradients versus refinement level l , for the randomly perturbed grids (Fig. 2c).

order accurate FVMs on a variety of grids. However, a number of gradient discretisation studies, e.g. [18, 19, 21–23], have focused on a particular type of grid which consists of very high aspect ratio cells over a curved boundary, as typically used for the simulation of high-speed boundary layer flows in aerodynamics. Although structured grids are usually employed, and therefore all the gradient schemes considered here, including the GG, are nominally second order accurate (first order at boundaries except the $q = 2$ schemes), very large errors have been observed. The LS methods have a particularly bad reputation, while the GG gradients are considered to perform better, although the aforementioned studies have shown that proper weighting can significantly improve the performance of LS gradients.

Figure 6 shows part of such a grid (the aspect ratio is reduced for clarity), which shall henceforth be referred to as HARC (High Aspect Ratio Curved grid). Usually, the differentiated variable’s contours more or less follow the shape of the boundary. The curvature introduces a nonlinearity that poses a challenge to gradient schemes like the ones considered here, which are founded on an assumption of linear variation of the variable in the neighbourhood of the cell. Furthermore, due to the large aspect ratio the magnitudes of the contributions of different faces can differ by several orders of magnitude, depending on the weighting scheme. The unweighted LS gradient, LS(-1), is particularly notorious. With reference to Fig. 6, LS(-1) places equal emphasis on satisfying $\Delta\phi_f = \nabla\phi(\underline{P}) \cdot (\underline{P}_f - \underline{P})$ for $f = 1$ (or 3) as for $f = 2$ (or 4). For $\gamma > 1$, where γ is the ratio of the y -displacement of \underline{P}_1 to that of \underline{P}_4 , both with respect to \underline{P} (Fig. 6), this results in the LS(-1) gradient underestimating the actual $\partial\phi/\partial y$ at \underline{P} by a factor of approximately γ . The resulting inaccuracy can be very severe, as in practical applications γ can be as high as 50 or greater [21]. Using proper weighting (inverse distance) greatly improves the accuracy.

So, we consider a HARC grid over a circular arc of radius $R = 1$, like the one shown in Fig. 6, whose spacing in the circumferential direction is $\Delta\theta_l = 0.256/2^l$ radians, for levels of refinement $l = 0, 1, \dots, 9$, while its radial spacing is $\Delta r_l = R \Delta\theta_l / A$ where $A = 1000$ is the cell aspect ratio. Grid level $l = 0$ has 2×2 cells, and grid level $l = 9$ has 1024×1024 cells in the (r, θ) directions. The first

most cases the results are identical, but for the LSA(1) and LS(2) schemes double precision proves insufficient beyond refinement level $l = 7$; with extended precision their nominal rate of convergence is fully recovered. The worst method in this respect is the LSA(2) method, for which double precision is insufficient beyond $l = 3$, and even extended precision is insufficient beyond $l = 7$. That LSA(2) is the worst performer in this respect is not surprising if one considers that it weighs neighbour contributions by inverse distance squared $\|\underline{R}_f\|^2$ and by the face area S_f ; since the neighbours in the circumferential direction (neighbours 1 and 3 in Fig. 6) are 1000 times farther away than neighbours in the radial direction (neighbours 2 and 4 in Fig. 6), and their corresponding faces are 1000 times smaller, the weight vectors \underline{V}_f for $f = 1$ and 3 have magnitudes $1000^3 = 10^9$ times smaller than those for $f = 2$ and 4. On the other hand, the same holds also for the TG(2) gradient, and yet it is stable, in double precision, down to the finest level $l = 9$. In this respect it even outperforms the LS(2) gradient, which starts to break down (in double precision) at the refinement level $l = 7$, even though it does not include face area weighting.

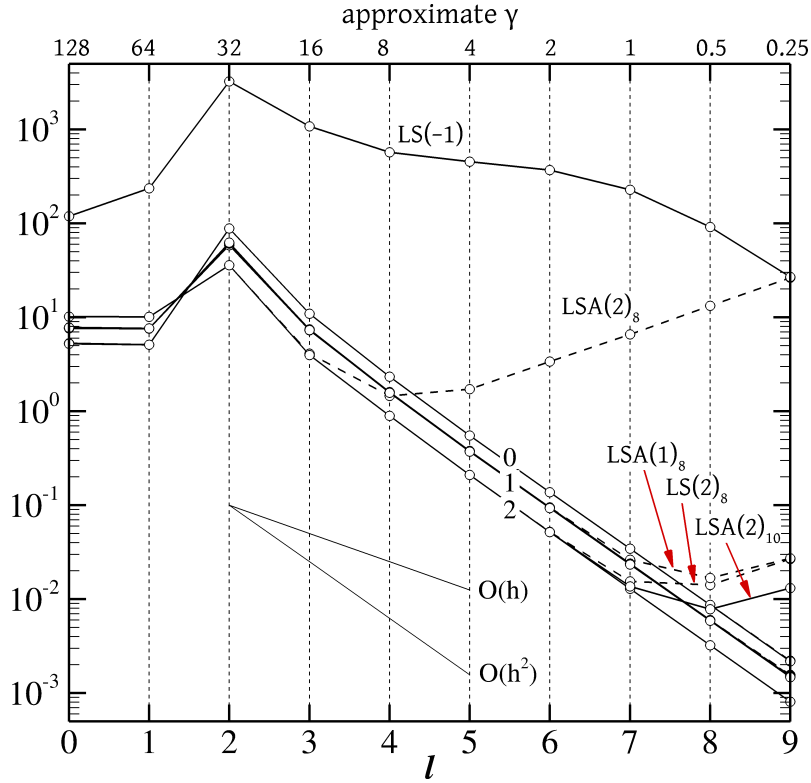


Figure 7: Mean errors of the tested gradient schemes when differentiating the radial function (17) on the HARC grid. Line group 0: TG(0), LSA(0). Line group 1: iTG(0), iTG(1), TG(1), iTG(2), GG, LS(1), LSA(1), GG+iTG(0), GG+LS(1). Line group 2: TG(2), LS(2), LSA(2).

Similar observations can also be made with respect to the maximum error, plotted in Fig. 8a. The gradient errors can again be grouped into the same groups 0, 1 and 2, with the errors of groups 0 and 1 reducing at a first-order rate because the respective gradients become first-order accurate at boundary cells. Group 2 includes the $q = 2$ gradients LS(2), LSA(2) and TG(2) which retain second order accuracy at boundary cells, and therefore even their maximum errors decrease at a second-order rate. However, the LSA(2) breaks down beyond $l = 3$ (beyond $l = 6$ in extended precision), as does the LS(2) beyond $l = 6$. The TG(2) double-precision does not break down until $l = 9$.

We also differentiated on the HARC grid a function that varies in the circumferential direction, as variables can vary in this direction as well (e.g. pressure along the length of an airfoil). The function

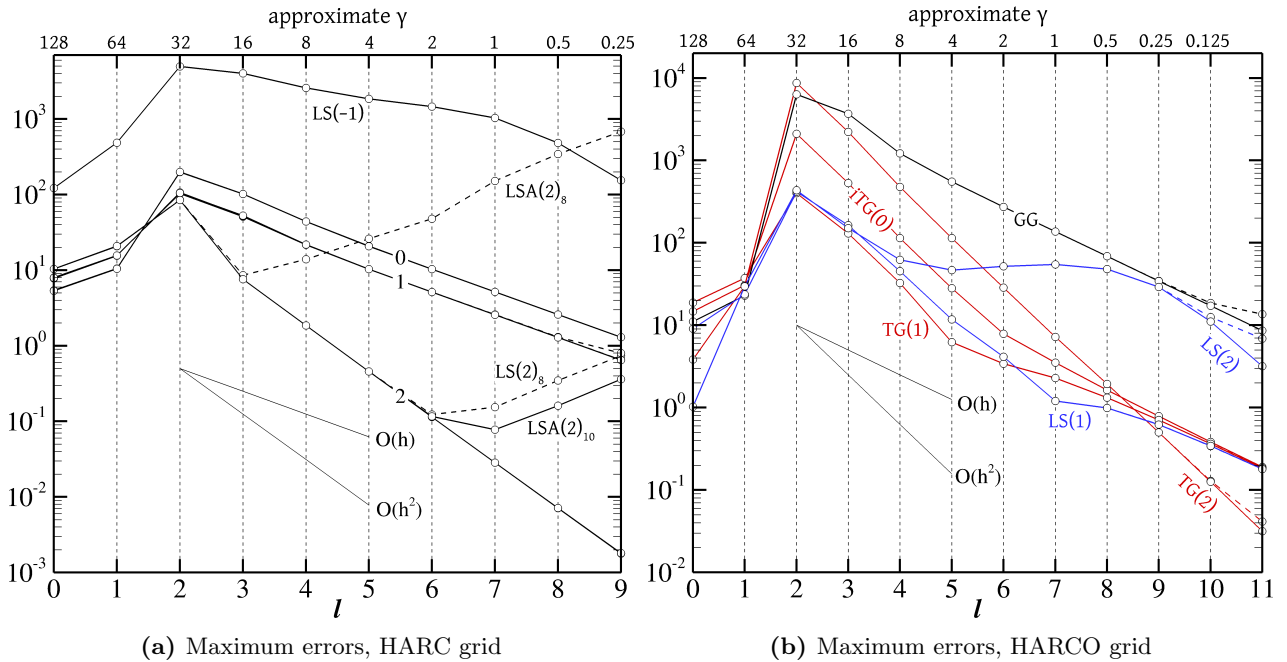


Figure 8: Maximum errors of different gradient schemes when differentiating the radial function (17) on (a) HARC grids and (b) HARCO grids. For the groups of lines denoted as 0, 1 and 2 in (a), see the caption of Fig. 7.

is

$$\phi(\theta) = \tanh(f(\theta)) \quad \text{where} \quad f(\theta) = f_{\min} + (f_{\max} - f_{\min}) \frac{\theta - \theta_{\min}}{\theta_{\max} - \theta_{\min}} \quad (18)$$

where $f_{\min} = 1$ and $f_{\max} = 3$ as before, while $\theta_{\min} = -0.512$ rad and $\theta_{\max} = +0.512$ rad are the extents of the domain in the circumferential direction. Thus, since our grids have an equal number of cells in the radial and circumferential directions, again ϕ as given by (18) varies from $\tanh(1)$ to $\tanh(3)$ across the same number of cells (1024 for $l = 9$) as when given by (17). Due to the high aspect ratio though, the distance over which ϕ given by (18) varies is $A = 1000$ times larger than that over which function (17) varies, which means that $\nabla\phi$ of (18) is about $A = 1000$ times smaller than that of (17).

In light of this we can interpret the errors plotted in Fig. 9. First of all, comparing Fig. 9a with 7 and Fig. 9b with 8a, we note that the pattern of errors of the differentiation of the circumferential function (18) is similar as for the radial function (17): the gradient errors form the same groups 0, 1 and 2, while the LS(-1) gradient stands out with its huge error. The errors in Figs. 9a and 9b are about 4 orders of magnitude smaller than those in Figs. 7 and 8a. Had the gradient schemes been equally effective in differentiating functions (18) and (17), the errors would have been only $A = 1000$ times smaller; therefore, differentiating function (18) poses a lesser challenge. This holds also with respect to the conditioning, as almost all of the gradients do not break down in double precision. Interestingly, only the GG gradient does break down beyond $l = 7$ (Fig. 9a).

Effect of oblique grid lines

Next, we repeated the experiments but on grids where the formerly radial group of grid lines has been rotated by an angle of 45° , as in the sketch of Fig. 10. We will refer to such grids as High Aspect Ratio Curved and Oblique (HARCO) grids. This time, the error curves do not fit so nicely into groups, so in order to avoid the cluttering the mean errors are drawn in separate plots of Fig. 11 according to

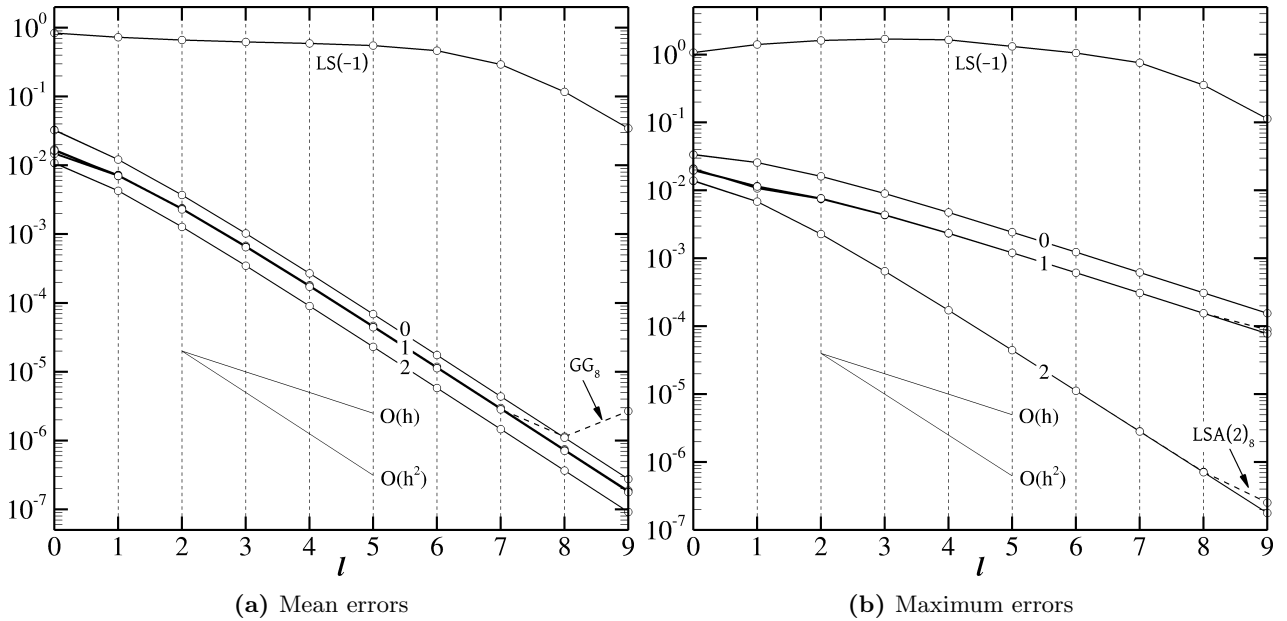


Figure 9: Mean (a) and maximum (b) errors of various gradient schemes for the differentiation of the circumferential function (18) on HARC grids. For the groups of lines denoted as 0, 1 and 2 see the caption of Fig. 7.

the gradient family: Fig. 11a (GG gradients), Fig. 11b (LS gradients), and Fig. 11c (TG gradients). A selected subset of all these are compared together in Fig. 11d. Maximum errors are plotted in Fig. 8b. On the HARCO grids we included two additional refinement levels, the finest one being $l = 11$ with 4096×4096 cells.

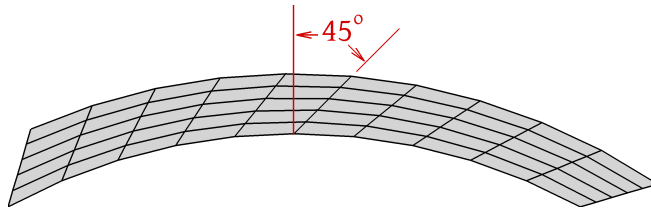


Figure 10: A High Aspect Ratio Curved Oblique (HARCO) grid.

Figures 11a and 11d show that on these grids the GG gradient is one of the worst performers, but skewness correction (GG+LS(1), GG+iTG(0)) brings it on a par with the best performing gradients, except on coarse grids ($l = 2, 3$). Of the LS schemes (Fig. 11b, LS(-1) is by far the worst, as usual, exhibiting its nominal second-order accuracy (because the grid is structured) only for $l \geq 8$. The LSA(2) is again very badly conditioned, breaking down beyond $l = 3$ in double precision and $l = 7$ in extended precision. The best among them appears to be the LS(1). The LS(2) does retain second-order accuracy at boundaries (Fig. 8b) but it exhibits this only at the finest levels, while overall its errors are relatively high. Furthermore, in double precision it breaks down beyond $l = 7$.

Of the TG gradients (Fig. 11c) the best performers are the TG(1) and TG(0), which are part of the group of best overall performers (TG(1), TG(0), LS(1), GG+iTG(0), GG+LS(1); only two of them are shown in Fig. 11d for clarity). It should be mentioned that iTG(1), while completely equivalent to TG(1) in exact arithmetic as shown in Sec. 4.2, was found to produce very large errors on levels $l \leq 4$ (not shown), while it becomes identical to the TG(1) for $l > 4$. A discrepancy between the iTG(1) and TG(1) gradients was not observed in previous tests. Unfortunately, the TG(2) gradient, which was the best performer thus far in previous tests, now performs poorly compared to most other schemes,

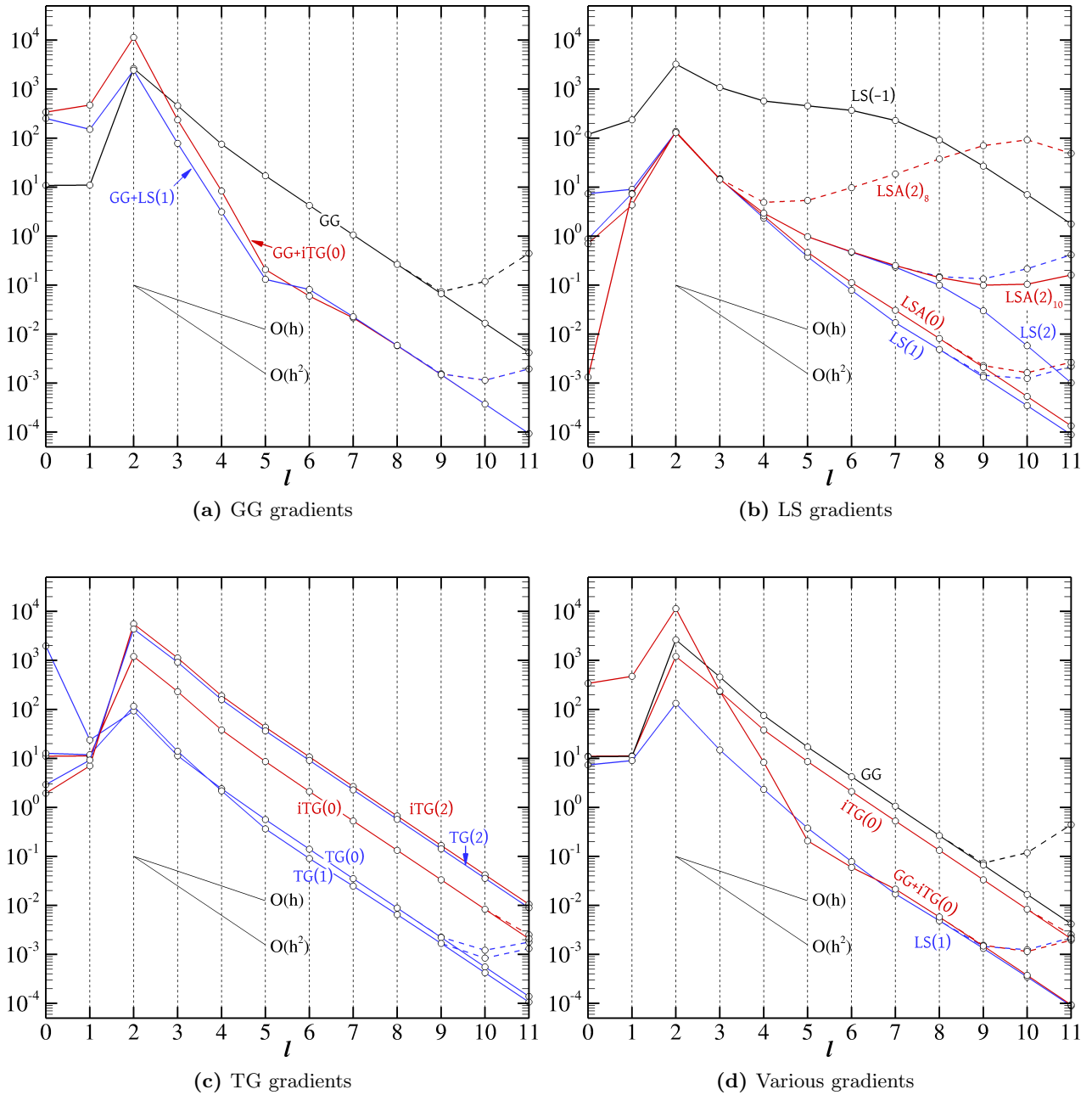


Figure 11: Mean errors of different gradient families on HARCO grids (Fig. 10) when differentiating the radial function (17).

despite being second-order accurate at boundaries (Fig. 8b). Interestingly, most of the gradients break down in double precision beyond $l = 9$ except for some which, however, have relatively large errors such as the LS(-1), iTG(2) and iTG(0) (GG is an exception: it is both inaccurate and ill-conditioned). Such breakdown is also not observed as much in the maximum error plots of Fig. 8b. It therefore seems that for breakdown to occur both the grid must be fine enough and the error must be low enough (“enough” being scheme-dependent).

Finally, Fig. 12 shows the mean and maximum errors of the differentiation of the circumferential function (18) by various gradient schemes on the HARCO grids. As for the HARC grids, these errors are more than 4 orders of magnitude smaller than the corresponding errors for the radial function (17), while the exact $\nabla\phi$ is only $A = 1000$ times smaller. Hence, the gradients do a better job differentiating function (18) than (17). The performance discrepancy between most schemes is less than that for the radial function (17). LS(-1) is once more by far the least accurate, while GG also lags behind the

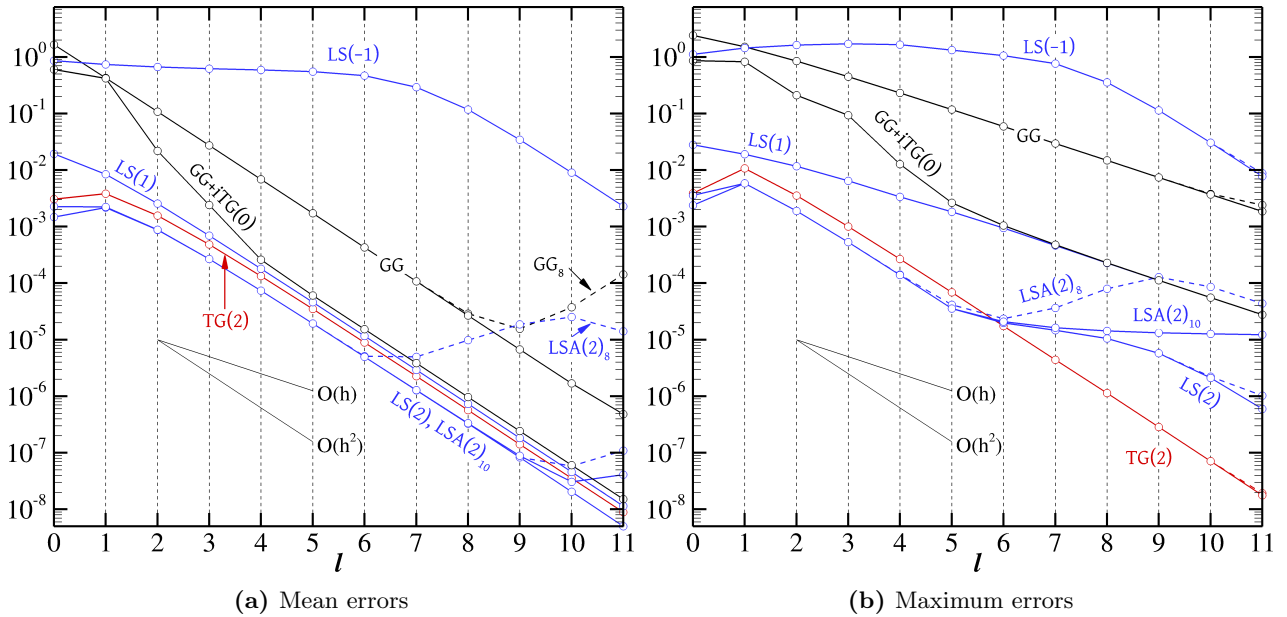


Figure 12: Mean (a) and maximum (b) errors of various gradient schemes for the differentiation of the circumferential function (18) on HARCO grids.

rest of the gradients significantly and furthermore breaks down in single precision beyond $l = 8$. The best accuracy is exhibited by the schemes LS(2) and LSA(2), but both of them, especially LSA(2), exhibit conditioning problems. The TG(2) follows in accuracy, and furthermore it does not exhibit conditioning problems.

6 Conclusions

A general framework for the construction of gradient discretisation schemes was presented. The LS gradients were shown to belong to this framework, and the TG gradients, where the weight vectors are normal to the cell's faces instead of in the direction of the neighbour cells' centroids, were proposed. The TG gradients have a number of attractive features: they are consistent, i.e. at least first-order accurate on all kinds of grids (unlike the GG gradients); they include area weighting which gives them an advantage over LS gradients on grids where there is significant variation in the sizes of a cell's faces (they retain a small advantage even if face area weighting is incorporated into the LS gradients); they have somewhat better conditioning (the LSA gradients can be particularly bad in this respect); and in terms of accuracy they usually rank among the top schemes in each of the tests conducted. The TG(2) ranked as the best or among the best schemes in all tests except, unfortunately, on the HARCO grids where its errors were rather large. The TG(1) and, perhaps surprisingly, the LS(1) gradients performed well on all tests, with the exception of LS(1) in the aforementioned case of composite grids where the sizes of a cell's faces vary significantly. Unfortunately, as mentioned, incorporation of the faces' areas into the weights (LSA) on the one hand does not completely restore the accuracy and on the other hand may introduce conditioning problems.

In the present work we only examined 2D grids composed of quadrilateral cells, while it is planned to test them also on grids of triangles and on 3D cases. In terms of skewness, unevenness and non-orthogonality, such grids present nothing new, as the effect of all these geometrical qualities on the order of accuracy of the gradient schemes has been determined theoretically and verified experimentally in the present work. In particular, all gradient schemes, except the GG, are first-order accurate

on triangular / tetrahedral grids (where favourable error cancellations between faces, such as those that can occur in quadrilateral / hexahedral grids to result in second-order accuracy, do not occur). However, a most challenging task is to compute the gradients on very high aspect ratio triangular / tetrahedral grids. In this case, often no close neighbours can be found in the radial direction among the cells that share a face with the current cell, which results in significant errors for both the GG and LS gradients, even if the latter are weighted, if only immediate neighbours are used in the computational stencil. The remedy has been found to be the inclusion of additional neighbours in the LS gradient stencil [22], among which certainly some can be found whose centroids lie close to the centroid \underline{P} across the radial direction. This strategy is not straightforward to incorporate into GG gradients, but is applicable to TG gradients as they are akin to LS gradients. The question then arises of what the weight vectors \underline{V}_f should be for these additional neighbours. One possibility is to use vectors aligned with the normal vectors of the faces of these neighbours which are crossed by the vectors $\underline{P}_{f^*} - \underline{P}$, where f^* now denotes the additional neighbour. This topic, along with the root cause of TG(2)'s poor behaviour on HARCO grids, forms part of our continuing investigations.

Acknowledgements

AS, YD and JT gratefully acknowledge funding from the LIMMAT Foundation, under the Project “MuSiComPS”.

References

- [1] P. Traoré, Y. M. Ahipo, and C. Louste, “A robust and efficient finite volume scheme for the discretization of diffusive flux on extremely skewed meshes in complex geometries,” *J. Comput. Phys.*, vol. 228, pp. 5148–5159, 2009.
- [2] I. Demirdžić, “On the discretization of the diffusion term in finite-volume continuum mechanics,” *Numer. Heat Transfer B*, vol. 68, pp. 1–10, 2015.
- [3] A. Jalali, M. Sharbatdar, and C. Ollivier-Gooch, “An efficient implicit unstructured finite volume solver for generalised Newtonian fluids,” *International Journal of Computational Fluid Dynamics*, vol. 30, no. 3, pp. 201–217, 2016.
- [4] J. H. Ferziger and M. Peric, *Computational methods for fluid dynamics*. Springer, 3rd ed., 2002.
- [5] A. M. Afonso, M. S. N. Oliveira, P. J. Oliveira, M. A. Alves, and F. T. Pinho, “The finite volume method in computational rheology,” in *Finite-Volume Methods – Powerful Means of Engineering Design*, ch. 7, pp. 141–170, In-Tech Open Publishers, 2012.
- [6] F. Pimenta and M. Alves, “Stabilization of an open-source finite-volume solver for viscoelastic fluid flows,” *Journal of Non-Newtonian Fluid Mechanics*, vol. 239, pp. 85–104, 2017.
- [7] A. Syrakos, Y. Dimakopoulos, and J. Tsamopoulos, “A finite volume method for the simulation of elastoviscoplastic flows and its application to the lid-driven cavity case,” *Journal of non-Newtonian Fluid Mechanics*, dec 2019.
- [8] T. J. Barth and D. C. Jespersen, “The design and application of upwind schemes on unstructured meshes,” in *AIAA Paper 89-0366*, 1989.

- [9] H. Jasak, *Error Analysis and Estimation for the Finite Volume Method with Application to Fluid Flows*. PhD thesis, Imperial College, London, 1996.
- [10] Ž. Lilek, S. Muzaferija, M. Perić, and V. Seidl, “An implicit finite-volume method using non-matching blocks of structured grid,” *Numer. Heat Transfer*, vol. 32, pp. 385–401, 1997.
- [11] J. Wu and P. Traoré, “Similarity and comparison of three finite-volume methods for diffusive fluxes computation on nonorthogonal meshes,” *Numer. Heat Transfer B*, vol. 64, pp. 118–146, 2014.
- [12] F. Moukalled, L. Mangani, and M. Darwish, *The Finite Volume Method in Computational Fluid Dynamics*. Springer, 2016.
- [13] T. J. Barth, “A 3-D upwind Euler solver for unstructured meshes,” in *AIAA Paper 91-1548-CP*, 1991.
- [14] S. Muzaferija and D. A. Gosman, “Finite-volume CFD procedure and adaptive error control strategy for grids of arbitrary topology,” *J. Comput. Phys.*, vol. 138, pp. 766–787, 1997.
- [15] C. Ollivier-Gooch and M. Van Altena, “A high-order-accurate unstructured mesh finite-volume scheme for the advection–diffusion equation,” *J. Comput. Phys.*, vol. 181, pp. 729–752, 2002.
- [16] F. Bramkamp, P. Lamby, and S. Müller, “An adaptive multiscale finite volume solver for unsteady and steady state flow computations,” *J. Comput. Phys.*, vol. 197, pp. 460–490, 2004.
- [17] A. Syrakos, S. Varchanis, Y. Dimakopoulos, A. Goulas, and J. Tsamopoulos, “A critical analysis of some popular methods for the discretisation of the gradient operator in finite volume methods,” *Physics of Fluids*, vol. 29, p. 127103, dec 2017.
- [18] E. Sozer, C. Brehm, and C. C. Kiris, “Gradient calculation methods on arbitrary polyhedral unstructured meshes for cell-centered CFD solvers,” in *AIAA Paper 2014-1440*, 2014.
- [19] N. Wang, M. Li, R. Ma, and L. Zhang, “Accuracy analysis of gradient reconstruction on isotropic unstructured meshes and its effects on inviscid flow simulation,” *Advances in Aerodynamics*, vol. 1, sep 2019.
- [20] M. Deka, S. Brahmachary, R. Thirumalaisamy, A. Dalal, and G. Natarajan, “A new green–gauss reconstruction on unstructured meshes. part i: Gradient reconstruction,” *Journal of Computational Physics*, oct 2018.
- [21] D. J. Mavriplis, “Revisiting the least-squares procedure for gradient reconstruction on unstructured meshes,” in *AIAA Paper 2003-3986*, 2003.
- [22] B. Diskin and J. L. Thomas, “Accuracy of gradient reconstruction on grids with high aspect ratio,” tech. rep., NIA Report No. 2008-12, 2008.
- [23] E. Shima, K. Kitamura, and K. Fujimoto, “New gradient calculation method for MUSCL type CFD schemes in arbitrary polyhedra,” in *AIAA Paper 2010-1081*, 2010.
- [24] L. J. Betchen and A. G. Straatman, “An accurate gradient and Hessian reconstruction method for cell-centered finite volume discretizations on general unstructured grids,” *Int. J. Numer. Methods Fluids*, vol. 62, pp. 945–962, 2010.